Structure, microstructure, and size dependent catalytic properties of nanostructured ruthenium dioxide

Pawel Nowakowski[a], Jean-Pierre Dallas[a], Sylvie Villain[a],
Agnieszka Kopia[b], Jean-Raymond Gavarri[a],*

[a]*Université du Sud Toulon Var, IM2NP, UMR CNRS 6242, BP 20132, 83 957 LA GARDE, France*
[b]*University of Science and Technology, AGH, Al. Mickiewicza 30, 30 059 Cracow, Poland*

Abstract

Nanostructured powders of ruthenium dioxide RuO_2 were synthesized via a sol gel route involving acidic solutions with pH varying between 0.4 and 4.5. The RuO_2 nanopowders were characterized by X-ray diffraction, scanning and transmission electron microscopy (SEM and TEM). Rietveld refinement of mean crystal structure was performed on RuO_2 nanopowders and crystallized standard RuO_2 sample. Crystallite sizes measured from X-ray diffraction profiles and TEM analysis varied in the range of 4–10 nm, with a minimum of crystallite dimension for pH = 1.5. A good agreement between crystallite sizes calculated from Williamson Hall approach of X-ray data and from direct TEM observations was obtained. The tetragonal crystal cell parameter (a) and cell volumes of nanostructured samples were characterized by values greater than the values of standard RuO_2 sample. In addition, the $[Ru–O_6]$ oxygen octahedrons of rutile structure also depended on crystal size. Catalytic conversion of methane by these RuO_2 nanostructured catalysts was studied as a function of pH, catalytic interaction time, air methane composition, and catalysis temperature, by the way of Fourier transform infrared (FTIR) spectroscopy coupled to homemade catalytic cell. The catalytic efficiency defined as FTIR absorption band intensities $I(CO_2)$ was maximum for sample prepared at pH = 1.5, and mainly correlated to crystallite dimensions. No significant catalytic effect was observed from sintered RuO_2 samples.
© 2008 Elsevier Inc. All rights reserved.

Keywords: Ruthenium dioxide; Sol gel process; Nanopowders; X-ray diffraction analysis; Rietveld structure analysis; Electron microscopy; Catalytic properties; Infrared spectroscopy

1. Introduction

Ruthenium dioxide presents a tetragonal rutile structure and a large variety of interesting properties. It is one of the best electronic conductive oxides [1–3]. It is a good catalyst as well as for reduction as for oxidation of specific gases [4–6]. This dioxide offers: (i) good thermal and chemical stabilities [7,8], (ii) strong resistance against chemical corrosion [9], and (iii) excellent chemical diffusion barrier [10]. In the area of microelectronics, RuO_2 was proposed as complementary metal–oxide–semiconductor (CMOS) component, and as electrode for DRAM (random access memory) capacitor [11,12].

It was also investigated as a catalyst for CO [13,14] or C_2H_4 [15,16] gas conversion. However, its capacity to convert methane into CO_2 and H_2O was never developed probably because of its high cost. Recently, many researches were concentrating on the development of new generations of gas sensors based on MOS technologies (metal–oxides–semiconductors) [17,18].

In previous works, we developed a series of studies on nanostructured catalytic ceria CeO_2 [19,20] and on ceria based thin films [21]. In the present work, we study correlations between crystal structure, microstructure, and catalytic conversion properties of RuO_2 nanopowders synthesized from a sol gel route depending on variable pH conditions. These RuO_2 based materials might be integrated into new miniaturized gas sensor devices.

*Corresponding author.

  E-mail address: gavarri.jr@univ-tln.fr (J.-R. Gavarri).

2. Experimental

In this section, we present first a specific sol gel elaboration method allowing preparing RuO_2 nanostructured powders having variable microstructure. Then, each synthesized nanostructured powder was characterized by X-ray diffraction and electron microscopy analysis. Finally, a homemade catalytic device was used to compare the catalytic conversion efficiency of air–methane gas mixtures by these nanopowders presenting various microstructures.

With regard to the potential pH data available in the literature [22], pH conditions should play a prominent role in our sol gel approach. So, we might expect some stabilization of various chemical species, for increasing values of pH: the main chemical species stable in water should be first Ru^{3+} ionic species (in acid solution), then Ru^{4+} species, and, finally, hydrated RuO_2 solid species.

2.1. Chemical precursors

Hydrate ruthenium (III) chloride ($RuCl_3$, xH_2O) 99.9% (PGM basis) was supplied by Alfa Aesar. Ammonia solution (NH_4OH) was supplied by Aldrich. Absolute ethanol (C_2H_5OH) was supplied by Carlo Erba Reagents.

2.2. Preparation of samples

Ruthenium dioxide precursor solution was prepared by dissolving the hydrate ruthenium (III) chloride, $RuCl_3$, xH_2O, in absolute ethanol. The solution was agitated for 24 h under air by the means of rotating magnet (400 rotations per minute). A dark brown colloidal solution (the sol) was obtained. At this step, acidic solution was obtained with pH = 0.4. After 7 days of ageing in room conditions, a wet gel was formed without any modification of pH and color. It should be noted that agitation process plays a prominent role by inserting oxygen in the liquid medium, and insuring a certain value of redox potential. Then, the next step consisted in adding well-controlled amounts of NH_4OH solution to this gel, in order to reach the following pH: 0.4, 1.5, 2.0, 3.0, and 4.5. It should be noted that, from pH 4.5, precipitation of $Ru(OH)_3$ started. As this hydroxide is unstable in presence of oxygen (from air), the precipitation of the RuO_2, xH_2O phase occurred, which was expected from the potential pH diagram data [23].

The wet gels were exposed to two successive cycles of heat treatment:

(1) in cycle 1, the wet gel was heated at a fixed temperature of 120 °C during 1 h: as a consequence, the solvent was completely evaporated and a new dark brown xerogel was formed and
(2) in cycle 2, this gel was heated at 450 °C for 2 h and, finally, anhydrous RuO_2 powder crystallized.

Finally, five samples, at five different pHs, were selected for structural, microstructural, and catalytic study. The samples were designated as RuO_2-n with $n = 1$–5, successively for pH = 0.4, 1.5, 2, 3, 4.5. A standard sample was prepared by heating a RuO_2 sample (pH = 1.5) at 800 °C for 10 h, under air. This sample will be noted as RuO_2-standard.

2.3. X-ray diffraction analysis

X-ray diffraction patterns were recorded on Siemens-Brucker D5000 equipment working in a classical θ–2θ angles coupled mode, with copper X-ray source ($\lambda = 1.5406$ Å), Soller slides, a secondary monochromator and a rotating sample holder. Structural refinements based on Rietveld method (RM) were performed making use of specific FullProf software [24–26] that allows calculating all structural parameters, including atom coordinates, profile parameters, from X-ray diffraction intensity profiles.

2.4. Electron microscopy

Morphologies and chemical composition (EDS) of the powder agglomerates were investigated using the scanning electron microscope (SEM) Philips XL30. For morphologies and crystals sizes/coherence lengths determination the transmission electron microscopy (TEM) observations were carried out using the TecnaiG2 microscope, operating at 200 kV, with LaB_6 source, equipped with CCD camera.

2.5. Catalytic analysis

The catalytic properties of these RuO_2 nanopowders in presence of air–CH_4 mixture were studied making use of Fourier transform infrared (FTIR) spectroscopy. The gas mixtures were supplied by Linde gas (methane conex high quality, R&D class 1). The equipment was an FTIR Unicam-Mattson spectrometer working with cube corner technology. Powder samples were first exposed to air–CH_4 action in a homemade heated cell (Fig. 1); then, the emitted gases were analyzed through the FTIR equipment.

The catalytic efficiency is relative to the proportion of CO_2 (and H_2O) resulting from classical reaction: $CH_4 + 2O_2 \rightarrow CO_2 + 2H_2O$. The reactor was constituted of a cylindrical cell in which the sample could be subjected to reactive air–methane flow. The sample temperature was controlled by a thermocouple, and stabilized at a given
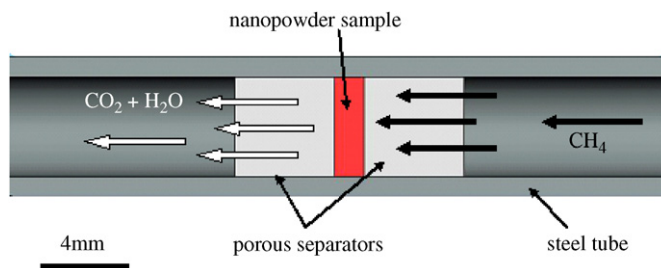

Fig. 1. Catalytic cell adapted to powder analysis. Analyses of air–methane flow at variable temperatures (2500 ppm CH_4, fixed speed of 10 cm^3/min).

T_{cat}-value corresponding to a given catalytic activity. The fixed mass (0.03 g for each test) of RuO_2 powder was placed between two porous (ZrO_2) separators (separators 1 and 2 (Fig. 1)).

The various gas flows, controlled by the flow meters (2500–100 ppm CH_4 in air), crossed through the separator 1, then the sample, finally the separator 2, with a fixed slow speed (10 $cm^3 min^{-1}$).

The cell was heated in a furnace at temperatures ranging between room temperature and 550 °C.

Preliminary studies were carried out at variable temperatures to determine background analysis.

Fig. 1 represents the homemade reactor cell. The emitted gases resulting from conversion of methane into CO_2 and H_2O were then led up to the FTIR spectrometer. The intensity variations of vibration adsorption bands of CH_4, CO_2, and H_2O molecules were then determined with FTIR records of 30 s with interval of 30 s. The catalytic conversion was analyzed at various fixed temperatures from 150 at 530 °C with interval of 20 °C. The catalytic efficiency was determined from surface measurements of the absorption bands of CH_4 and CO_2 at a certain time t of gas–solid interaction: in fact, these intensities are determined for a given time of FTIR measurement, while a permanent flow crossed through the sample. For a fixed time t and a given temperature T_{cat}, the catalytic efficiency was defined as being proportional to the intensity of CO_2 peak $I(CO_2)$. The FTIR intensities of CH_4 absorption peaks were shown to linearly vary with air–methane composition (notes as Φ_{CH_4} in ppm). This value $I(CO_2)$ is directly linked to the derivative dX/dt of total CO_2 amount X, which was formed during the conversion reaction, and depending itself on time t. In other terms, the integral of the curve dX/dt should directly deliver the total amount of CO_2 associated with CH_4 conversion by the system.

3. Results

3.1. Structural characterizations

The XRD analyses were carried out for all samples, and then the diffraction patterns were indexed and diffraction profiles were refined from RM [27,28], using the FullProf software analysis adapted to X-ray diffraction. Each refinement calculation was performed with similar parameters. For rutile structure (with space group $P4_2/mnm$), the Wyckoff atomic positions are, respectively: Ru (2*a*: 0, 0, 0/$\frac{1}{2}$, $\frac{1}{2}$, $\frac{1}{2}$) and O (4*f*: x, x, 0/$\frac{1}{2}-x$, $\frac{1}{2}+x$, $\frac{1}{2}$/$\frac{1}{2}+x\frac{1}{2}-x\frac{1}{2}/-x$, $-x$, 0). So, the main refined parameters were the two tetragonal cell parameters (a and c), one oxygen coordinate and two mean Debye–Waller factors. These Debye–Waller factors ($B_{iso} = 8\pi^2/3\langle\Delta u\rangle^2$ with $\langle\Delta u\rangle$ representing mean atom thermal vibrations or static distortions due to defects), were calculated as being mean global factors for Ru and O atoms: the refinement of individual values for Ru and O did not deliver any improvement of refinement results.

The occupancy factors of Ru and O atoms (n_{occ}) were first fixed to expected values of 0.5 and 1. Then, they were released at the end of Rietveld calculations: their refined values were stabilized close to initial stoichiometric values, without any improvement of refinement results.

The profile parameters were the classical U, V, W parameters of Lorentzian like approach proposed by the software. A texture parameter was also taken into account.

The diffraction patterns of RuO_2-n samples (observed and calculated profiles, obtained for various pH) and of standard crystallized RuO_2 sample are reported, respectively, in Figs. 2a–e and 3. As it should be remarked especially for sample RuO_2-4 (Fig. 2d), a relatively poor fit is obtained for the (210) reflection: this might be due to complexity of crystallite population in such samples, with presence of diversified anisotropic nanosized crystals. In fact, the FULLPROF software cannot take into account the three parameters, anisotropy, size effect, and microstrain.

The various refined parameters are listed in Table 1. The classical R factors determining the quality level of refinement are reported in this table (see table note for definitions).

At the end of refinement calculations, we used the Williamson–Hall (W–H) plot representations [29,30] to extract size effect noted D_{hkl} (or coherence length), depending on crystal direction, and distortion effect (ε_{hkl}), also depending of crystal direction.

The W–H plots (Fig. 4) were obtained using the mathematical relation (1):

$$\frac{\Delta(2\theta)\cos(\theta)}{\lambda} = \frac{1}{D_{hkl}} + 2\varepsilon_{hkl}\left(\frac{2\sin\theta_{hkl}}{\lambda}\right) \quad (1)$$

and reporting the experimental values $Y = \Delta(2\theta)\cos\theta$ and $X = 2\sin\theta/\lambda$ on a graph (Y, X).

In these expressions:

- D_{hkl} is the average crystallite size or coherence length depending on hkl indices;
- $\Delta(2\theta) = (\Delta(2\theta)_{sample} - \Delta(2\theta)_{standard})$ is the contribution of size effect and distortion to the full width at half maximum (FWHM) of Bragg peaks (hkl), assuming that profiles are strictly Lorentzian;
- θ is the Bragg angle;
- $\Delta(2\theta)_{sample}$ is the observed FWHM of the Bragg peak;
- $\Delta(2\theta)_{standard}$ is the instrumental contribution obtained from crystallized RuO_2 sample;
- λ is the X-ray wavelength; and
- $\varepsilon_{hkl} = \Delta d/d$ is the microstrain due to defects.

The instrumental $\Delta(2\theta)_{standard}$ values were determined from profile analyses of the highly crystallized RuO_2-standard sample (Fig. 3).

In Figs. 4a–e, W–H plots of RuO_2-n nanostructured samples are reported. The (101) peaks were included in our estimation because of they relatively strong intensities. The (310) Bragg peaks having weak intensities (Figs. 2b–d),
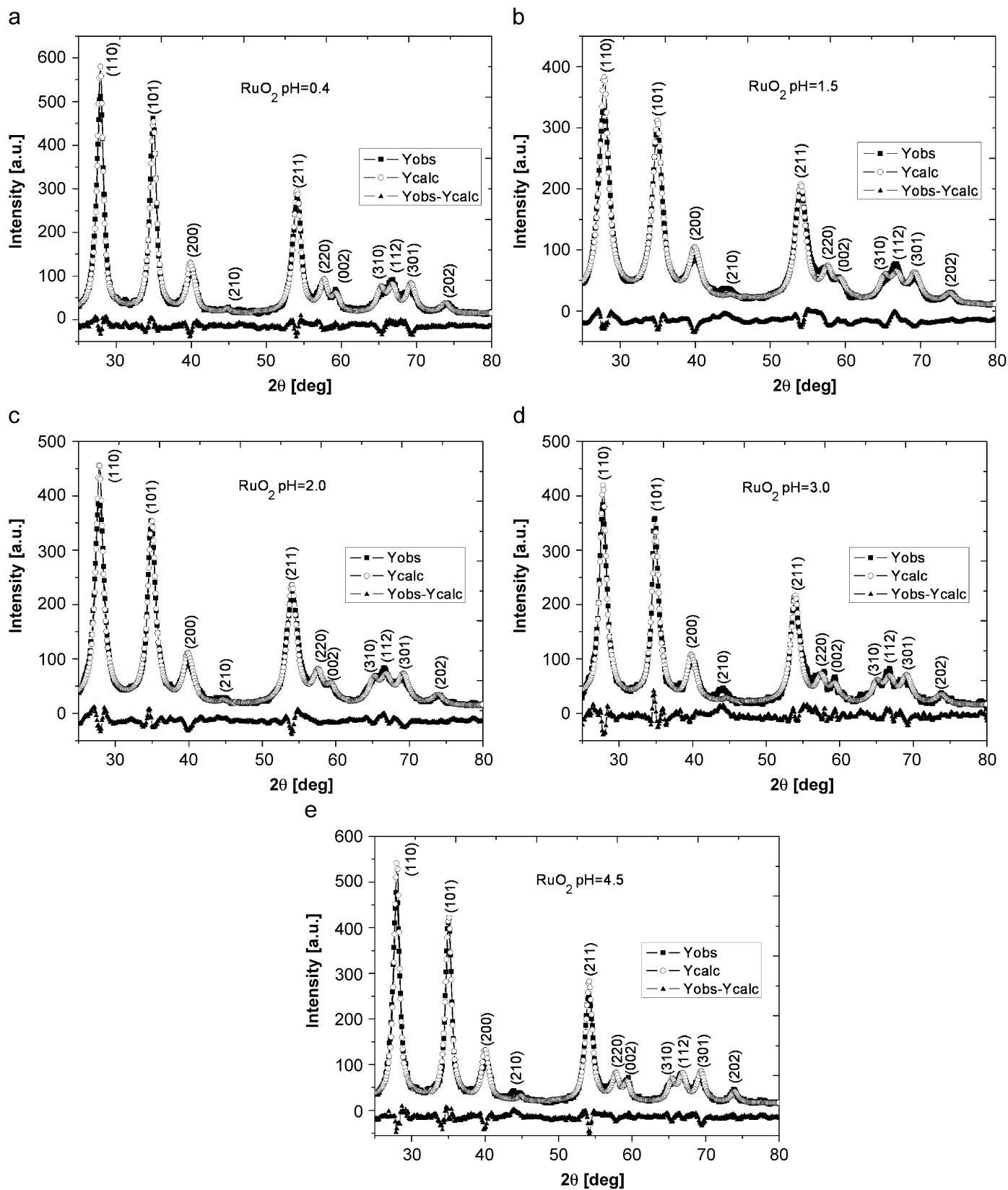
Fig. 2. X-ray diffraction patterns of RuO$_2$-*n* samples (Rietveld method: *Y* observed ■ and *Y* calculated—○) at: (a) pH = 0.4, (b) pH = 1.5, (c) pH = 2.0, (d) pH = 3.0, and (e) pH = 4.5. ▲—(difference: *Y* observed− *Y* calculated).

present abnormal FWHM values (Figs. 4b–d). These abnormal values are generally associated with large dimensions of crystal or small distortions. It is the reason why they were excluded from our D and ε determinations. For the same reasons, the (301) peak for RuO$_2$-2 sample (Fig. 2b) and (112) peak for RuO$_2$-3 sample (Fig. 2c) is removed from our estimations.
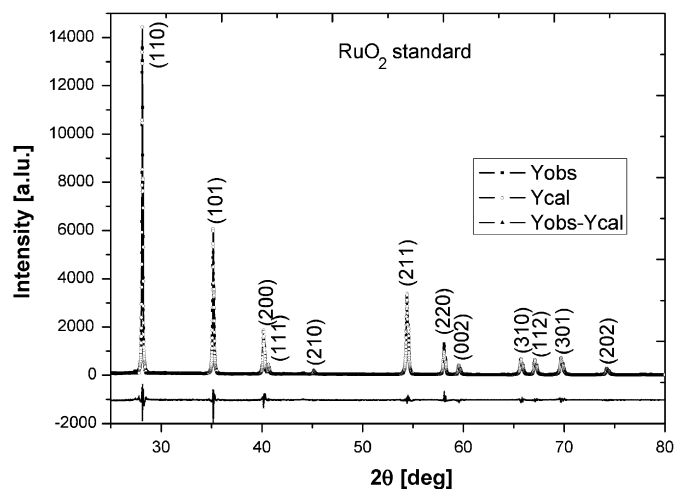

Fig. 3. X-ray diffraction pattern of standard RuO$_2$ prepared by heating RuO$_2$ sample (pH = 1.5) at 800 °C for 10 h, under air. (Rietveld method: ■—Y observed–experimental data, ○—Y calculated values), and ▲—(difference: Y observed–Y calculated).

It should also be noticed that, for the RuO$_2$ samples obtained at pH = 1.5, 2.0 (Figs. 2b and c), the (002) Bragg peaks are large; however, they are thin for the samples prepared at pH = 0.4, 3.0 and 4.5 (Figs. 2a and d). In the case of RuO$_2$ sample prepared at pH = 3.0, the very low value of FWHM should result from a strong anisotropy of nanocrystal with elongated dimension in the c-axis direction.

These correlations gave the final values of D_{hk0} (and ε_{hk0}) corresponding to size effect (and distortions) in directions perpendicular to the c-axis of rutile structure. In fact, the complexity of W–H plots was probably due to certain anisotropy of distortions and presence of elongated nanocrystals with c-axis parallel to the longest dimension.

Table 2 reports the various interatomic distances d_1 (Ru–O bond in [110] direction), d_2 (out of (001) plane) and Ru–Ru (along octahedron chains of rutile structure), the calculated W–H D_{hkl} and ε_{hkl} values. The ratio d_1/d_2 characterizing the oxygen octahedron anisotropy is reported: it is weaker than 1 for nanosized powders, and close to 1 for crystallized sample (in which oxygen octahedrons should be quasi-isotropic). Our results obtained for crystallized samples are in good agreement with the ones previously published by Hazen et al. [31]; however, the cell parameters and the ratio d_1/d_2, obtained for nanosized samples, are significantly different from the corresponding parameters obtained for large crystals.

Table 1
Structural parameters refined from Rietveld calculations from powder diffraction data for each RuO$_2$-n sample

	RuO$_2$-1:pH = 0.4	RuO$_2$-2:pH = 1.5	RuO$_2$-3:pH = 2.0	RuO$_2$-4:pH = 3.0	RuO$_2$-5:pH = 4.5	RuO$_2$-micro
a (10^{-10}m) (σ_a)	4.516	4.521	4.518	4.527	4.519	4.4904
	(0.001)	(0.001)	(0.001)	(0.001)	(0.001)	(0.0001)
c (10^{-10}m) (σ_c)	3.113	3.111	3.105	3.111	3.116	3.1040
	(0.001)	(0.001)	(0.001)	(0.001)	(0.001)	(0.0001)
x (O) (σ_x)	0.298	0.297	0.298	0.305	0.313	0.312
	0.002	0.002	0.002	0.003	0.003	0.002
B_{iso} (10^{-20} m^2) (σ_B)	0.96	1.20	0.54	0.55	1.32	0.46
	0.15	0.26	0.19	0.26	0.13	0.08
n_{occ} (Ru)	0.5	0.5	0.5	0.5	0.5	0.5
n_{occ} (O)	1.0	1.0	1.0	1.0	1.0	1.0
UVW (profile)	5.831	5.342	4.842	4.342	3.342	0.250
	−5.248	−5.842	−6.441	−7.041	−8.241	−0.255
	0.673	0.843	0.373	0.173	0.260	0.471
R factor	1.86	2.76	1.92	2.87	2.61	2.43
R_p profile (%)	10.3	11.5	9.80	13.6	13.2	18.8
R_{wp} (%)	12.3	14.2	11.4	16.9	15.6	23.7
R_e (%)	15.5	16.6	15.8	17.3	17.4	6.65
χ^2 (%)	0.64	0.73	0.52	0.95	0.842	15.7
Zero shift	0.029	0.022	−0.031	0.024	0.026	0.018
Displacement	0.002	0.002	−0.002	0.004	0.175	0.005

Notes: n_{occ}: occupancy factors. Wyckoff positions: Ru (2a); O (4f); 1 Å = 10^{-10} m, R—crystallographic R-factor: $R = 100 \frac{\sum_h |F_{obs,h} - F_{calc,h}|}{\sum_h |F_{obs,h}|}$, R_p—profile factor: $R_p = 100 \frac{\sum_{i=1,n} |y_{i\,obs} - y_{i\,calc}|}{\sum_{i=1,n} |y_{i\,obs}|}$, R_{wp}—weighted profile factor: $R_{wp} 100 \left[\frac{\sum_{i=1,n} w_i |y_{i\,obs} - y_{i\,calc}|^2}{\sum_{i=1,n} w_i y_{i\,obs}^2} \right]^{1/2}$, R_{exp}—expected weighted profile factor: $R_{exp} = 100 \left[\frac{(n-p)}{\sum_i w_i y_{i\,obs}} \right]^{1/2}$, χ^2—chi-square function of fit: $\chi^2 = \sum_i w_i \{y_{i obs} - y_{i calc}\}^2$ [25].
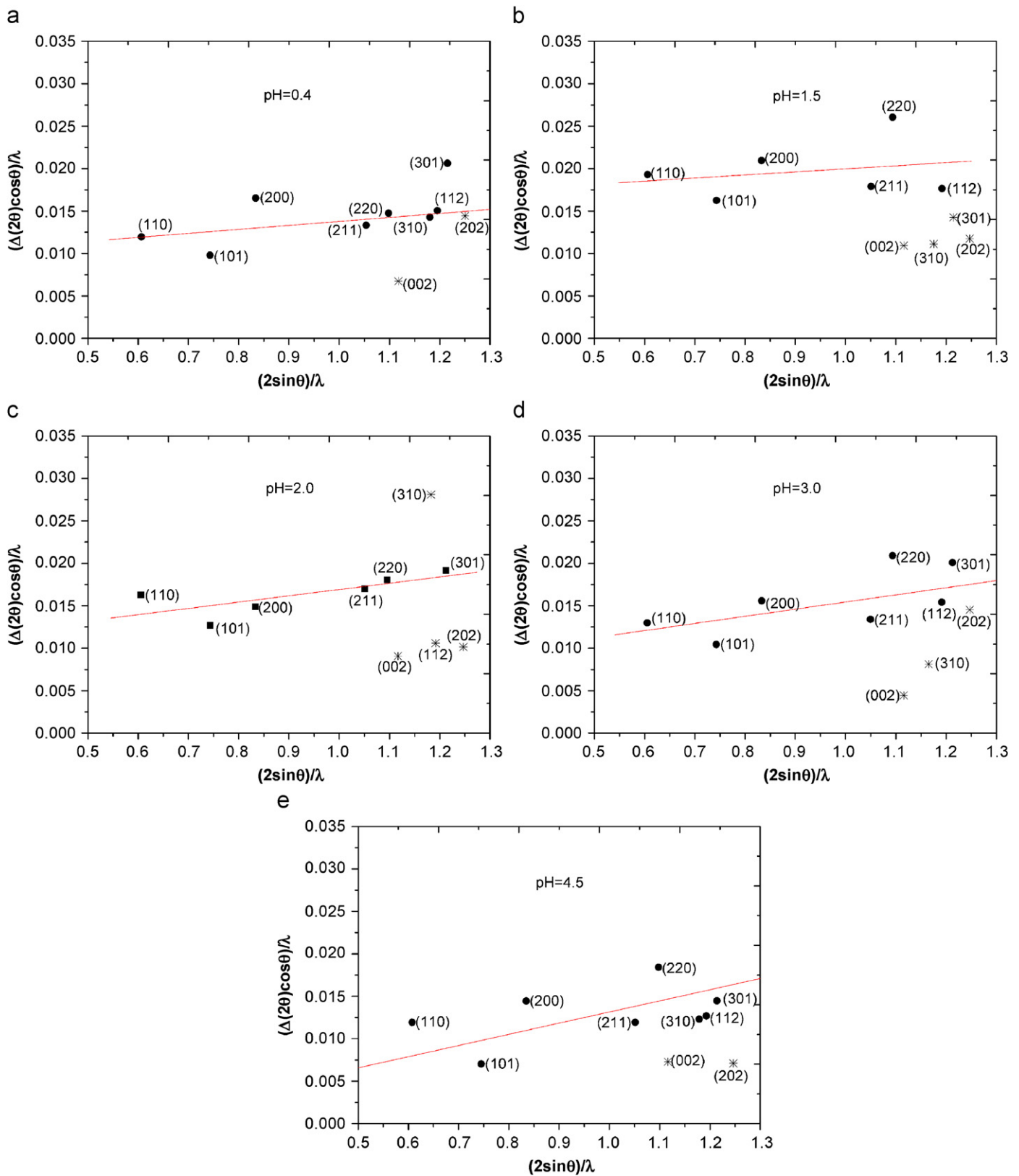
Fig. 4. Williamson–Hall plots for RuO$_2$-n samples: (a) pH = 0.4, (b) pH = 1.5, (c) pH = 2.0, (d) pH = 3.0, and (e) pH = 4.5. ●—values included in the D (crystals size or coherence lengths) estimation, and ∗—values eliminated from linear correlations of W–H plots.

Table 2
Structural and microstructural data for RuO_2-n samples

Sample-n pH	Cell volume V in $(10^{-10}\,m)^3$	Ru–O bond length d_1 (in [110] crystal direction) in $10^{-10}\,m$	Ru–O bond length d_2 (out of (00l) plane) in $10^{-10}\,m$	Ratio d_1/d_2	Ru–Ru bond length	Size D (Williamson–Hall) (nm)	Distortion (Williamson–Hall) ε
RuO_2-1:pH = 0.4	63.494	1.895	2.021	0.938	1.556	11	0.0023
RuO_2-2:pH = 1.5	63.612	1.897	2.021	0.938	1.555	8	0.0047
RuO_2-3:pH = 2.0	63.420	1.897	2.017	0.940	1.552	10.5	0.0037
RuO_2-4:pH = 3.0	63.773	1.948	1.991	0.978	1.555	12	0.0032
RuO_2-5:pH = 4.5	63.654	1.992	1.962	1.015	1.558	16.5	0.0036
RuO_2-micro	62.597	1.972	1.957	1.007	1.552	250	0.0008

3.2. Role of pH on structure and microstructure

3.2.1. Cell parameters, size, and distortions

From Table 1, some significant modifications in structural parameters can be observed. In the RuO_2-n series, the cell parameter a is close to $a = 4.52 \times 10^{-10}\,m$ while this parameter is significantly smaller for standard RuO_2 sample ($a = 4.49 \times 10^{-10}\,m$). Taking into account the experimental errors, the difference between these values is quite significant.

In Table 2, the various calculated D and ε values are reported for each sample. The main result resides in the fact that a minimum of crystal size and maximum of crystal distortion is observed for pH = 1.5. Fig. 5 shows the evolution of D versus pH.

3.2.2. Atom coordinates

The oxygen coordinate x varies with pH: from $n = 1$–5, it increases from $x = 0.298$ to 0.31 and, for standard sample, $x = 0.31$. In Table 2, these variations involve significant evolutions of the two Ru–O distances: as pH increases, the Ru–O bond length (d_1) located in (a_1, a_2) plane of rutile structure increases, while the other distance of the $[RuO_6]$ octahedron (d_2) decreases. In other terms, in RuO_2-n nanostructured samples, the $[RuO_6]$ octahedrons should be anisotropic with a ratio $d_1/d_2 < 1$, while, in crystallized samples (grain sizes greater than 1000 nm), these octahedrons should be quasi-isotropic with a ratio $d_1/d_2 \geqslant 1$.

To try to interpret such a correlation between small dimension (couple D, ε) and bond lengths or oxygen octahedron modifications, we should assume that, for nanocrystals, the chemical bonds located at the crystal surface, associated with intrinsic metallic properties of RuO_2, should present strong modifications in nature and spatial extension. In other terms, some electron redistribution should occur at the surface of crystal, involving a relaxation of interatomic distances in the crystal core. Such an hypothesis has to be validated by other approaches.

3.3. Microstructural analysis

To better understand the variation of D and ε values with pH, we carried out scanning and TEM.
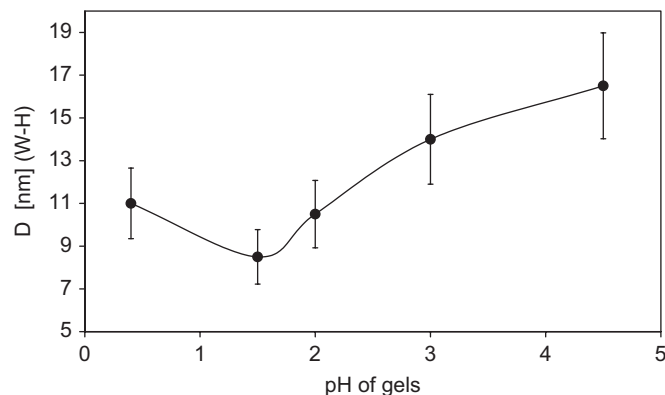

Fig. 5. Crystal size (or coherence length) evolution of RuO_2-n samples versus pH of gels.

3.3.1. Scanning electron microscopy

Figs. 6a–e represent the SEM images (secondary electron) of the RuO_2-n powders. At the micrometric scale of SEM techniques, large agglomerates are observed: in Figs. 6a, c, and d (for pH = 0.4, 2.0 and 3.0), very small grains (0.2 µm) coexist with large platelets. For pH = 1.5 (Fig. 6b), grain shapes and dimensions are more uniform. For pH = 4.5 (Fig. 6e), large blocks are observed.

3.3.2. Transmission electron microscopy

The RuO_2 nanoparticles were imaged by means of TEM. For TEM analyses, standard copper grids associated with ultrathin carbon films were used to fix small quantities of powder by simple contact with RuO_2-n samples. Then the statistical analyses of crystal size distribution were performed from 20 TEM images of each RuO_2-n powder sample (Table 3). Figs. 7a and b show general aspect of RuO_2 powder morphology at pH = 0.4, 1.5, 2.0, 4.5 (Fig. 7a), and strong shape anisotropy (Fig. 7b) of grain for RuO_2 obtained at pH 3.0. Figs. 7c–g present a selection of these analyses. One can observe RuO_2-n crystal grains having quasi-rectangular shapes and diameters D ranging from 8 at 14 nm. Each value of size D is associated with relative proportion of crystals having similar size (noted C in % in the table). Couples of values (D, C) are reported (with D in nm).
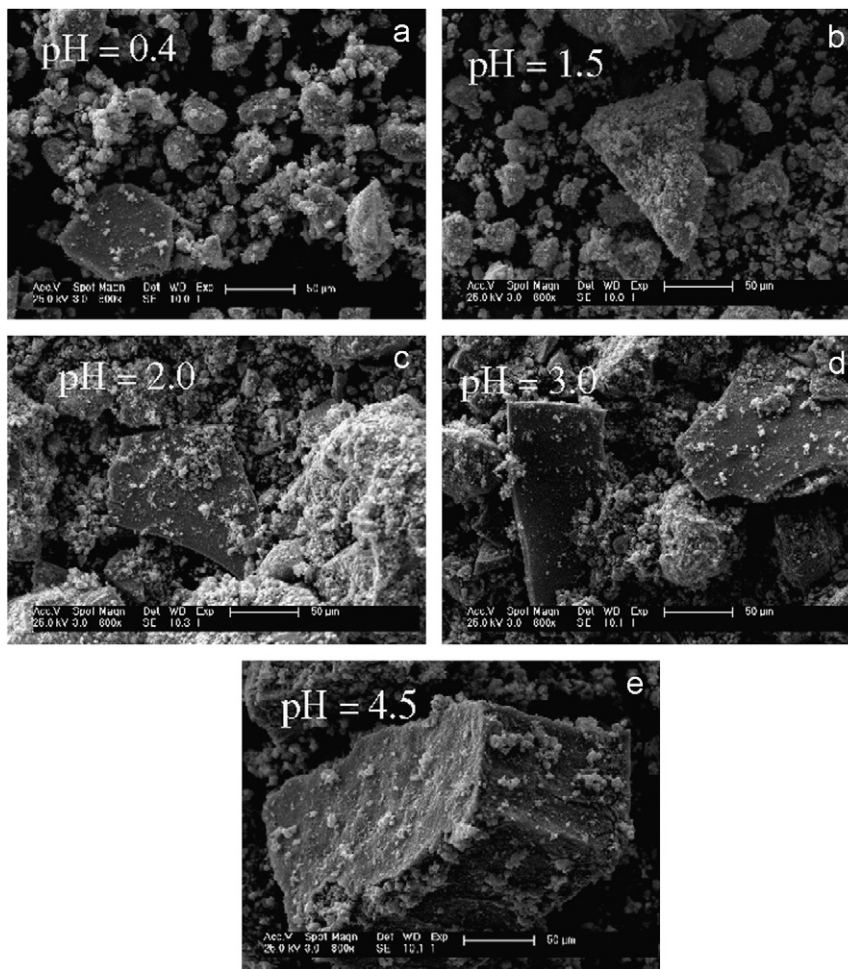
Fig. 6. Scanning electron microscopy images of RuO_2-n series: (a, c, d) small RuO_2-1,3,4 grains with large platelets, (b) uniform small grains of RuO_2-2, and (e) RuO_2-5 large blocks.

Table 3
Size distribution from TEM statistical analyses: D—size in nm, C (%)—proportion of crystal belonging to same dimension range

RuO_2	$n = 1$, pH = 0.4	$n = 2$, pH = 1.5	$n = 3$, pH = 2.0	$n = 4$, pH = 3.0	$n = 5$, pH = 4.5
D, C (%)	6, 2	4, 8	6, 16	9, 5	12, 10
D, C (%)	7, 10	5, 11	7, 22	10, 9	13, 13
D, C (%)	8, 16	6, 17	8, 24	11, 7	14, 12
D, C (%)	9, 18	7, 17	9, 19	12, 19	15, 15
D, C (%)	10, 22	8, 20	11, 11	13, 13	16, 15
D, C (%)	11, 7	9, 11	12, 4	14, 33	17, 25
D, C (%)	12, 8	10, 6	13, 2	15, 16	20, 4
D, C (%)	13, 3	11, 5	17, 2		40, 5
D, C (%)	14, 3	12, 3		D_{hk0}/D_{001}	
D, C (%)	15, 3	13, 1		50/15, 3	
D, C (%)	16, 5	16, 1		70/20, 2	
D, C (%)	20, 3			120/30, 2	
D, C (%)				200/50, 2	
$\langle D \rangle$	12	9	11	13	15

The double symbol D/D for pH = 3 designates anisotropic dimensions. D_{hk0}, D_{001}—directions of anisotropic grains belonging to $(hk0)$ planes and perpendicular to these planes.

In the case of sample at pH = 3.0, it was necessary to report two values associated with anisotropic crystallites (D_{hk0} and D_{001} should be the sizes, respectively, perpendicular to c-axis and along the c-axis of rutile cell—Fig. 7b).

The same influence of pH on the RuO_2 nanopowders crystallization can be observed as in the case of the XRD/W–H calculations (Fig. 8).

The size distribution (Table 3) extracted from TEM observations and the $\langle D \rangle$ (mean average) values agree well with X-ray diffraction data extracted from W–H approach. It should be remarked that, given this heterogeneous distribution of nanocrystal sizes, the interpretation of our diffraction profiles in terms of unique distribution of couples (D, ε) might be necessarily incomplete: in fact, the ε values calculated from W–H model might also partly reflect this diversity of sizes.

From these TEM analyses, we clearly established that the crystallite sizes of samples present an evolution in agreement with XRD data with a minimum of size for pH = 1.5. Fig. 8 compares the D parameter evolutions obtained from XRD approach and TEM analysis. The
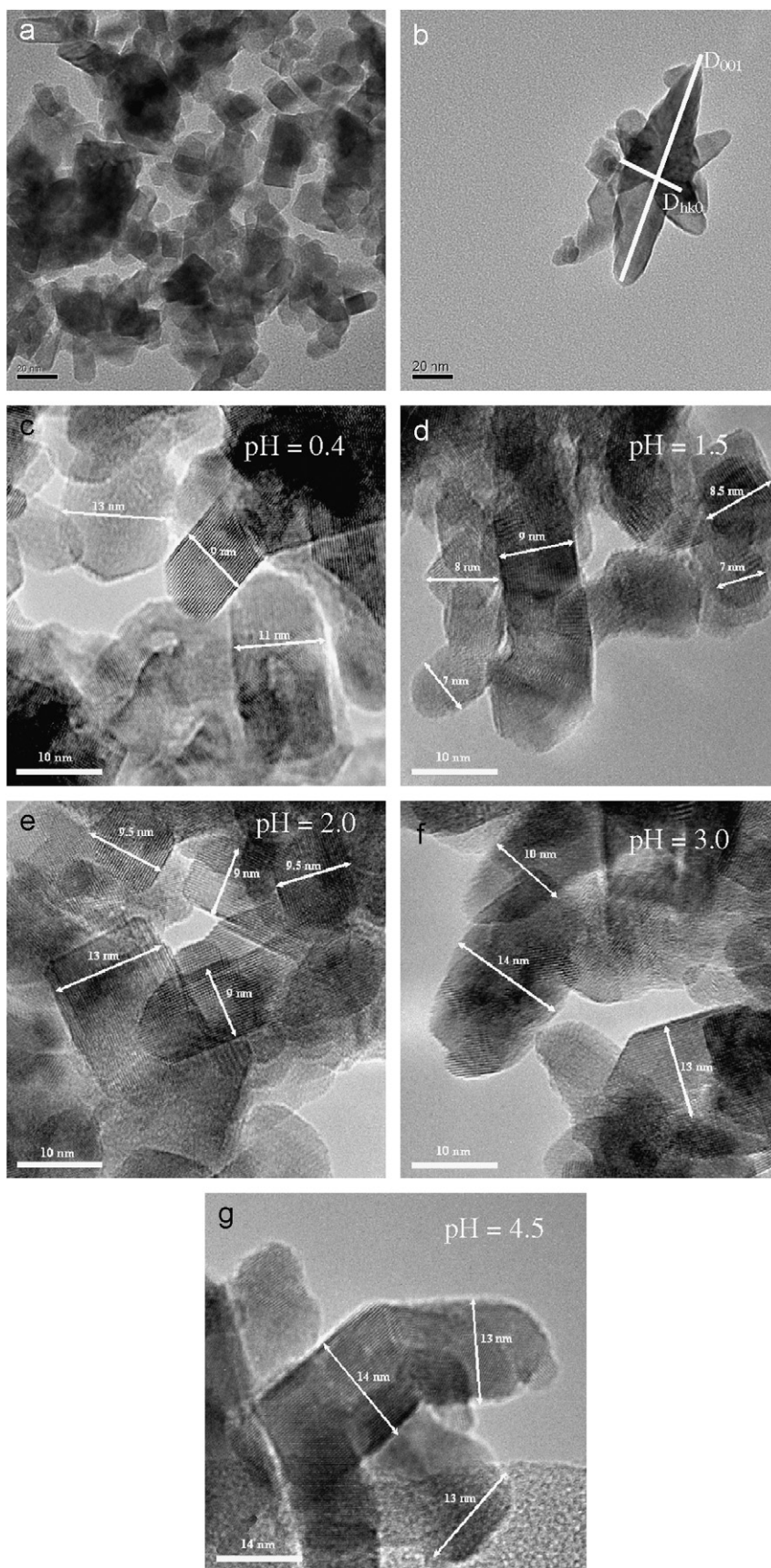
Fig. 7. (a–g) TEM images of RuO$_2$-n series: sizes of nanoparticles. (a) General aspect of RuO$_2$ grains morphology obtained at pH = 0.4, 1.5, 2.0, 4.5; (b) strong shape anisotropy of grain for RuO$_2$ obtained at pH 3.0; and (c–g) RuO$_2$ (prepared at various pH) crystal grains of rectangular shapes and size measurements.
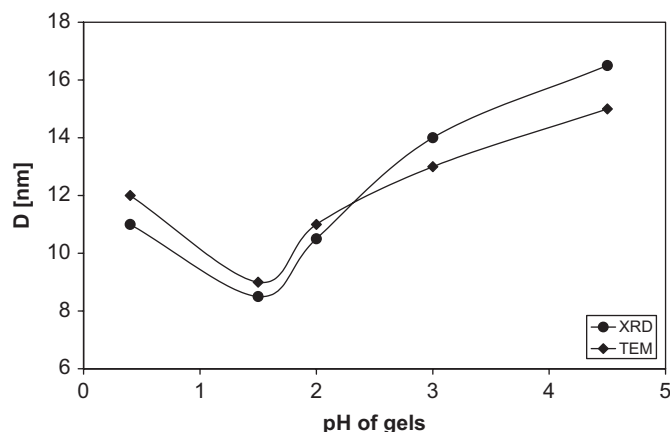
Fig. 8. Comparison of crystal sizes (or coherence lengths) D_{XRD} obtained from XRD and $\langle D \rangle_{TEM}$ mean values from TEM observation techniques. ●—D_{XRD} values calculated from W–H approach (XRD), and ◆—$\langle D \rangle_{TEM}$ mean values obtained from TEM observations.

detailed analyses of size distribution delivered additional information: each RuO$_2$-n sample is characterized by a large diversity of crystal sizes. This might be an additional factor playing a role in Bragg peak shapes: this size distribution might have some influence on the as-determined distortions ε.

3.4. Catalytic properties

Fig. 9 shows infrared spectroscopy analyses carried out on system without and with nanostructured RuO$_2$ at 350 °C ($m_{RuO_2} = 0.03$ g). In absence of any catalytic matter a maximum intensity of methane vibration bands is observed, while, in presence of RuO$_2$ powder, the transformation of methane into CO$_2$ and water takes place. When RuO$_2$ powders are subjected to pure air flow without any CH$_4$ gas, no CO$_2$ and H$_2$O gases are detected. The I(CO$_2$) intensity integral was used as the parameter "dX/dt" defining the catalytic efficiency at time t. No catalytic conversion was significantly observed from the crystallized standard sample obtained after sintering at 800 °C.

The catalytic efficiency (defined as dX/d$t = I_{cat}(t, T)$), depending on catalysis temperature T_{cat} in the range of 150–525 °C, is reported in Fig. 10. This catalysis efficiency is thermally activated. Depending on pH, it reaches various saturation levels, at different saturation temperatures noted T_{sat}. The best catalytic efficiency is obtained for pH = 1.5 with $T_{sat} = 425$ °C. For pH = 3 and 4.5, the saturation level intensity is weaker than the one at pH = 1.5, and the associated saturation temperature is of about 500 °C. Samples with pH = 0.4 and 2 give intermediate results for saturation levels and temperatures.

In Fig. 11, we have reported the values of catalytic efficiency dX/dt, as a function of exposition time t, for one sample at pH = 0.4 and for various CH$_4$ contents (noted Φ_{CH_4} expressed in ppm units) in air–CH$_4$ flows. The saturation level for $T_{cat} = 350$ °C varies with CH$_4$ content
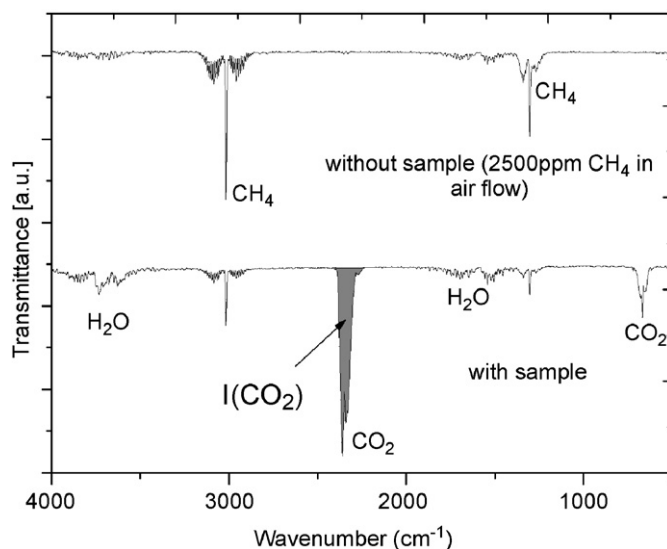

Fig. 9. FTIR spectroscopy of emitted gases: without any catalytic sample, and in presence of a RuO$_2$-2 catalyst at fixed temperature $T_{cat} = 350°$ (CH$_4$ converted into CO$_2$ and H$_2$O). The dX/d$t = I$(CO$_2$) intensity represents the catalytic efficiency.
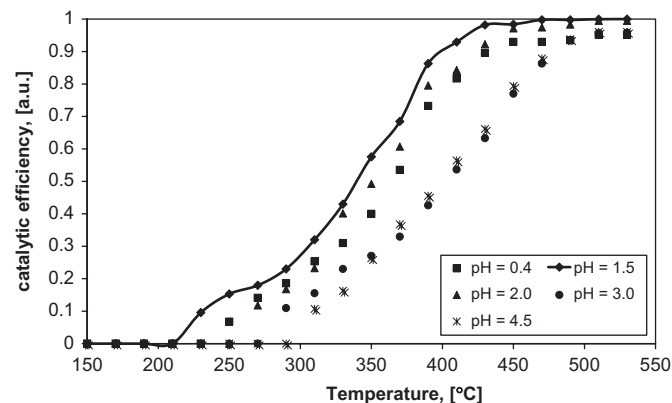

Fig. 10. Catalytic efficiency in presence of CH$_4$ (2500 ppm) gas flow reported as a function of catalysis temperature (from 150 at 525 °C), for RuO$_2$-n nanopowders samples prepared from gels with variable pH.

in air–methane flow following the relation:

$$(dX/dt)_{sat} = 2.73 \times 10^{-4} \Phi_{CH_4} + 0.123$$
$$\times \text{(reliability coefficient 0.999)}.$$

The efficiency increases linearly with ppm content in CH$_4$. However, for zero ppm CH$_4$, the extrapolation of the curve should deliver an artificial residual value of dX/d$t = 0.123$, probably due to both experimental errors and non-linear absorption of CH$_4$ on solid at very low CH$_4$ content in air–gas mixture.

No catalytic activity was observed during a first duration of 8 min for each sample (Figs. 11 and 12): this is due to progressive introduction of gas mixture in the device. The intensities of FTIR methane bands are functions of this initialization period of about 8 min: they first increase then,
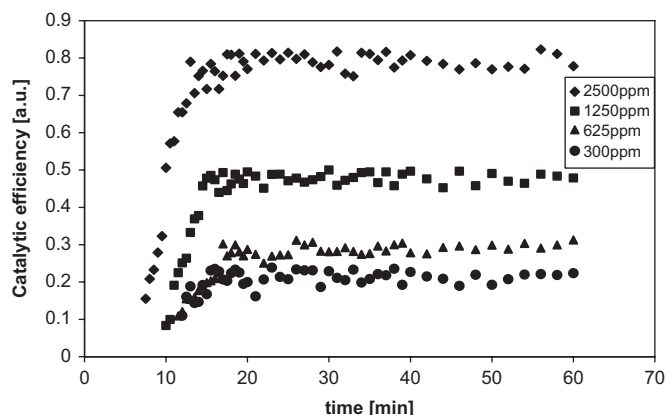
Fig. 11. Catalytic efficiency of RuO$_2$-1 sample as a function of time t for various methane concentrations Φ_{CH_4} (from 300 at 2500 ppm) at $T_{cat} = 350\,°C$.

Fig. 12. Catalytic efficiency reported as a function of pH and time t of RuO$_2$-n samples at $T_{cat} = 350\,°C$.

after this period, they reach a constant value, which also corresponds with the beginning of catalytic conversion and CO$_2$ production.

On Fig. 12, we report the catalytic efficiency dX/dt as a function of time, for various pH (flow being fixed at 2500 ppm/CH$_4$): it is clearly shown that the saturation level of catalytic efficiency at 350 °C is maximum for pH = 1.5, and the lowest efficiency is observed for pH = 4.5. These maximum and minimum efficiency values are well correlated with the crystallite sizes given by XRD and TEM analyses.

Fig. 13 shows that catalytic efficiency reaches a maximum value at pH = 1.5, which is also characterized by the largest specific surface ($1/D$). These efficiency and specific surface are similar for samples at pH = 0.4 and 2.0.

4. Conclusions

Structure refinements performed on nanostructured RuO$_2$-n samples and standard RuO$_2$ powder showed that the rutile structure presented some modifications, directly related to crystallite sizes and/or distortion. The cell volume is larger in nanosized sample than in crystallized ones. This result is a good agreement with results found on CeO$_2$ oxide by Zhang et al. [32]. For CeO$_2$, the lattice parameter increased up to 0.45% as the particle size decreased to 6 nm, as observed with X-ray diffraction. Raman spectra also suggested the particle-size effect and concomitant lattice expansion. The lattice expansion was interpreted by the authors in terms of increased concentrations of point defects with decreasing particle size.

These nanosized samples present anisotropic oxygen octahedrons while in crystallized samples these octahedrons are quasi-isotropic. A very good agreement was obtained between D values extracted from W–H calculations and direct observations from TEM analyses. The anisotropy of crystallites suggested by the abnormal shape of (002) Bragg peak is partly confirmed by TEM analyses for samples $n = 1, 3, 4, 5$. These modifications might be related to modifications of chemical bonds at the surface of
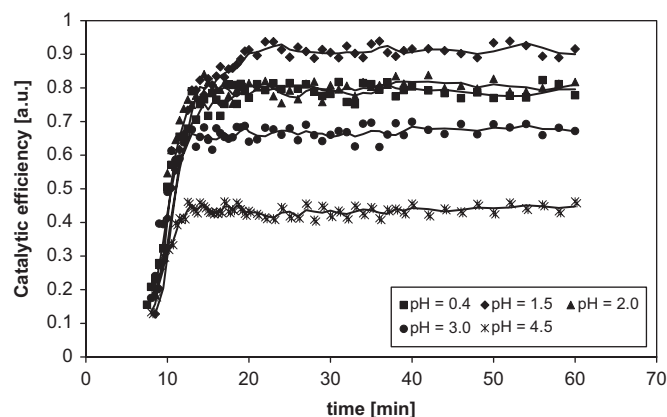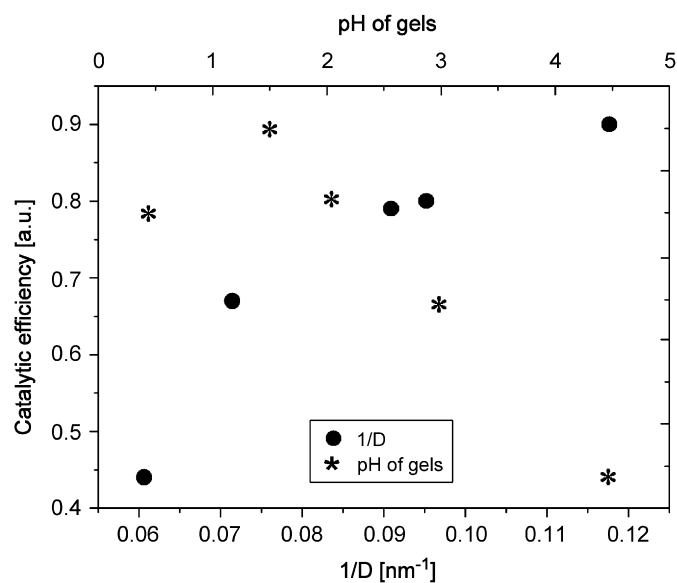

Fig. 13. Evolution of catalytic efficiency as a function of pH (crystal sizes/coherent lengths) and specific surface $1/D$ (D values calculated from W–H model). Maximum of catalytic efficiency was observed for the RuO$_2$ nanopowder obtained at pH = 1.5, i.e. for the smallest crystallite sizes.

nanocrystals. As an elemental approach, this crystal cell expansion might be associated with softening of chemical bonds due to surface effect.

The strong catalytic activity of nanostructured RuO$_2$ materials interacting with air–methane flow was linked to various parameters (pH of sol gel precursor, grain sizes, temperature, air–methane flow composition). For pH = 1.5, size D reaches a minimum, and, correlatively, a maximum value of conversion rate is observed. This result cannot be attributed to the sole low D values: probably, these D values should be closely correlated to increasing specific surfaces and porosity in RuO$_2$ powders. SEM analyses argue in favor of smaller agglomerates for pH = 1.5. In other terms, pH conditions should govern, first, local crystal growth (giving rise to nanosized crystals)

and, second, kinetics of agglomeration of such nanosized crystals.

Acknowledgments

References

[1] K. Frolich, V. Cambel, M. Machajdik, Mater. Sci. Semicond. Process. 5 (2003) 173–177.

[2] V.E. Jalenkovic, K.Y. Tong, W.Y. Cheung, S.P. Wong, Microelectron. Eng. 71 (2004) 237–241.

[3] J.H. Huang, J.S. Chen, Thin Solid Films 382 (2001) 139–145.

[4] H. Over, M. Muhler, Prog. Surf. Sci. 72 (2003) 3–17.

[5] K. Reuter, M. Scheffler, Phys. Rev. Lett. 90 (2003).

[6] J.-M. Zen, A.S. Kumar, J.-Ch. Chen, J. Mol. Catal. A Chem. 165 (2001) 177–188.

[7] S.H. Oh, C.G. Park, C. Park, Thin Solid Films 359 (2000) 118–123.

[8] K.L. Jiao, Q.X. Jia, W.A. Anderson, Thin Solid Films 227 (1993) 59–65.

[9] L. Armelao, D. Barreca, B. Moraru, J. Non-Cryst. Solids 316 (2003) 364–371.

[10] P.C. Liao, S.Y. Mar, W.S. Ho, Y.S. Huang, K.K. Tiong, Thin Solid Films 287 (1996) 74–79.

[11] K. Frohlich, J.C. Hooker, M. Francuilli, A. Dimoulas, F. Roozeboom, Mater. Sci. Eng. B 109 (2004) 117–121.

[12] J.J. Kim, D.H. Jung, M.S. Kim, Thin Solid Films 409 (2002) 28–32.

[13] S. Wendt, A.P. Seitsonen, H. Over, Catal. Today 85 (2003) 167–175.

[14] J. Wang, C.Y. Fan, K. Jacobi, G. Ertl, J. Phys. Chem. B 106 (2002) 5476–5482.

[15] S. Wodiunig, V. Patsis, C. Comninellis, Solid State Ionics 136–137 (2000) 813–817.

[16] U.A. Paulus, Y. Wang, H.P. Bonzel, K. Jacobi, G. Ertl, Surf. Sci. 566–568 (2004) 989–994.

[17] N. Sabate, J. Cerda, C. Cane, Sensors Actuators B 107 (2005) 688–694.

[18] N. Yamazoe, Sensors Actuators B 108 (2005) 2–14.

[19] S. Villain, Ch. Leroux, J. Musso, J.R. Gavarri, A. Kopia, M. Klimczak, J. Kusinski, J. Metastable Nanocryst. Mater. 12 (2002) 59–69.

[20] S. Saitzek, S. Villain, J.R. Gavarri, Mater. Sci. Forum Trans. Tech. Publ. 513 (2006) 1–14.

[21] M. Chmielowska, A. Kopia, C. Leroux, S. Saitzek, J. Kusinski, J.-R. Gavarri, Solid State Phenom. 99–100 (2004) 235–238.

[22] J. Malek, A. Watanabe, T. Mitsuhashi, Thermochim. Acta 282/283 (1996) 131–142.

[23] F. Mousset, Ph.D. Work, ed. 388, Chimie Physique et Chimie Analytique de Paris-Centre, 2004.

[24] T. Roisnel, J. Rodriguez-Carvajal, in: R. Delhez, E.J. Mittenmeijer (Eds.), Conference (EPDIC 7), 2000, pp. 118–123.

[25] J. Rodríguez-Carvajal, Abstracts of the Satellite Meeting on Powder Diffraction of the XV Congress of the International Union of Crystallography, Toulouse, 1990, 127pp.

[26] J. Rodríguez-Carvajal, Newsletter 26 (2001) 12–19.

[27] V.K. Pecharsky, P.Y. Zavalij, Springer Science + Business Media, Inc., 2003.

[28] J. Rodriguez-Carvajal, INV02, Chester (England), July 10–14, 1995.

[29] G.K. Williamson, W.H. Hall, Acta Metall. 1 (1953).

[30] A. Sarkar, P. Mukherjee, P. Barat, Mater. Sci. Eng. A (2007).

[31] R.M. Hazen, L.W. Finger, J. Phys. Chem. Solid (1981) 143–151.

[32] F. Zhang, S.-Wa. Chan, J.E. Spanier, E. Apak, Q. Jin, R.D. Robinson, I.P. Herman, Appl. Phys. Lett. 0 (2002) 127–129.